

1                   **Capillary processes increase salt**  
2                   **precipitation during CO<sub>2</sub> injection in saline**  
3                   **formations**

4                   **Helena L. Kelly<sup>1</sup>, Simon A. Mathias<sup>1†</sup>**

5                   <sup>1</sup>Department of Earth Sciences, Durham University, Durham, UK

6                   (Received 2018-06-29)

7   An important attraction of saline formations for CO<sub>2</sub> storage is that their high salinity  
8   renders their associated brine unlikely to be identified as a potential water resource in the  
9   future. However, high salinity can lead to dissolved salt precipitating around injection  
10  wells, resulting in loss of injectivity and well deterioration. Earlier numerical simulations  
11  have revealed that salt precipitation becomes more problematic at lower injection rates.  
12  This article presents a new similarity solution, which is used to study the relationship  
13  between capillary pressure and salt precipitation around CO<sub>2</sub> injection wells in saline  
14  formations. Mathematical analysis reveals that the process is strongly controlled by a  
15  dimensionless capillary number, which represents the ratio of the CO<sub>2</sub> injection rate  
16  to the product of the CO<sub>2</sub> mobility and air-entry pressure of the porous medium. Low  
17  injection rates lead to low capillary numbers, which in turn are found to lead to large  
18  volume fractions of precipitated salt around the injection well. For one example studied,  
19  reducing the CO<sub>2</sub> injection rate by 94% led to a tenfold increase in the volume fraction  
20  of precipitated salt around the injection well.

† Email address for correspondence: s.a.mathias@durham.ac.uk

## 21 1. Introduction

22 An important aspect of many international CO<sub>2</sub> emissions reduction plans involves  
23 storing CO<sub>2</sub> within the pore space of brine-containing aquifers, often referred to as saline  
24 formations (Nordbotten & Celia 2006; MacMinn *et al.* 2010). The reason for choosing  
25 saline formations as opposed to freshwater aquifers is the idea that brine is sufficiently  
26 saline that it is unlikely to be suitable for exploitation as a future water resource. However,  
27 the dissolved salt within the brine can lead to operational problems (Miri and Hellevang  
28 2016).

29 When CO<sub>2</sub> is injected into a saline formation, there is a high interfacial area between  
30 the CO<sub>2</sub> and the brine. Consequently, there is dissolution of CO<sub>2</sub> into the brine and  
31 evaporation of the water into the CO<sub>2</sub>-rich phase (Spycher *et al.* 2003). Surrounding  
32 the injection well, a dry-out zone develops where the water in the brine is completely  
33 evaporated. A consequence of this evaporation is that the dissolved salt precipitates  
34 as a solid phase, leading to significant loss of permeability around the injection well.  
35 Ultimately, this process can lead to complete deterioration of the injection well (Miri  
36 and Hellevang 2016).

37 A number of numerical modeling studies have been undertaken to investigate impor-  
38 tant controls on salt precipitation in the dry-out zone. Zeidouni *et al.* (2009) derived  
39 an analytical solution using method of characteristics (MOC) to estimate the volume  
40 fraction of precipitated salt in the dry-out zone (hereafter referred to as  $C_{30}$ ) due to CO<sub>2</sub>  
41 injection in saline formations. They concluded that the distribution of precipitated salt  
42 was uniform within the dry-out zone.

43 An important limiting assumption was that there is a local pressure equilibrium be-  
44 tween the CO<sub>2</sub>-rich and aqueous phases. The difference between the pressures of a non-  
45 wetting and wetting phase (the CO<sub>2</sub>-rich and aqueous phases, respectively, in this con-

46 text) is referred to as the capillary pressure. Pruess and Muller (2009) explored the same  
47 problem using the numerical reservoir simulator, TOUGH2, with the CO<sub>2</sub> storage mod-  
48 ule, ECO2N (Pruess and Spycher 2007). When capillary pressure is set to zero,  $C_{30}$  is  
49 found to be insensitive to injection rate. However, when capillary pressure is accounted  
50 for,  $C_{30}$  is found to increase with reducing CO<sub>2</sub> injection rate.

51 A physical explanation is provided as follows (Pruess and Muller 2009): capillary pres-  
52 sure is significantly increased as the wetting saturation is reduced. This can lead to  
53 a reversing in the direction of the wetting pressure gradient, which in turn results in  
54 counter-current flow, whereby brine flows in the opposite direction to the injected CO<sub>2</sub>.  
55 The counter-current flow provides additional brine to the dry-out zone leading to an  
56 increased availability of salt for precipitation. The counter-current flow rate is driven  
57 by phase saturation gradients. As the injection rate increases, the counter-current flow  
58 becomes less significant in comparison.

59 Kim *et al.* (2012) extended the work of Pruess and Muller (2009) by performing a  
60 wider sensitivity analysis. They found that the value of  $C_{30}$  was significantly increased  
61 for scenarios involving high permeability and low injection rates. Furthermore, contrary  
62 to Zeidouni *et al.* (2009), they found that  $C_{30}$  was non-uniform, with the highest values  
63 present at the edge of the dry-out zone. This localized increase in salt precipitation is  
64 attributed to the combined effects of gravity and capillary pressure driven counter-current  
65 flow.

66 Li *et al.* (2013) found that smoother capillary pressure curves lead to faster dissolution  
67 of CO<sub>2</sub> into the aqueous phase. This is presumably because smoother capillary pressure  
68 curves lead to more capillary diffusion of the CO<sub>2</sub>-rich phase and hence greater interfacial  
69 area between the CO<sub>2</sub>-rich phase and the aqueous phase.

70 The suite of numerical simulations described by Pruess and Muller (2009) and Kim *et*

71 *al.* (2012) have provided significant insight into the processes that control salt precipita-  
72 tion during CO<sub>2</sub> injection in saline formations. However, probably due to the perceived  
73 computational expense of numerically simulating this problem to an adequate accuracy,  
74 a more widespread sensitivity analysis has not been undertaken to further understand  
75 this process.

76 Analytical solutions have been developed to better understand many other aspects of  
77 the CO<sub>2</sub> storage process. Nordbotten & Celia (2006) developed a similarity solution to  
78 study the propagation rate of a CO<sub>2</sub> plume and its associated dry-out zone during injec-  
79 tion of CO<sub>2</sub> into a cylindrical saline formation. Hesse *et al.* (2007, 2008) and MacMinn *et*  
80 *al.* (2010, 2011) developed MOC solutions to study the migration of CO<sub>2</sub> plumes follow-  
81 ing the cessation of injection. Mathias *et al.* (2011a) extended the analytical solution of  
82 Nordbotten & Celia (2006) to estimate the resulting pressure buildup within an injection  
83 well. Mathias *et al.* (2011b) combined the work of Mathias *et al.* (2011a) and Zeidouni  
84 *et al.* (2009) to study the role of partial miscibility between the CO<sub>2</sub> and brine on pres-  
85 sure buildup. More recently, Mathias *et al.* (2014) derived a MOC solution to estimate  
86 the temperature distribution around a CO<sub>2</sub> injection in a depleted gas reservoir. There  
87 are many other such examples in the literature. However, all the analytical solutions  
88 presented to date revolve around the CO<sub>2</sub> transport problem reducing to a hyperbolic  
89 partial differential equation (PDE), such that MOC or some variant can be used for the  
90 solution procedure. The difficulty of accounting for capillary pressure is that this leads to  
91 a diffusive component within the equations, rendering MOC inadequate in this regard.

92 Unrelated to CO<sub>2</sub> storage, McWhorter and Sunada (1990) derived a similarity solution  
93 to look at two-phase immiscible flow around an injection well, which explicitly captures  
94 the counter-current flow associated with capillary pressure effects. In the past, their  
95 solution has not been commonly used due to difficulties with evaluating the necessary

96 non-linear multiple integrals associated with their equations (Fucik *et al.* 2007). However,  
97 more recently, Bjornara and Mathias (2013) have provided a more efficient evaluation  
98 procedure by re-casting the equations as a boundary value problem, which they then  
99 solve using a Chebyshev polynomial differentiation matrix (Weideman and Reddy 2000).

100 The objective of this study is to use the method of Bjornara and Mathias (2013) and  
101 extend the similarity solution of McWhorter and Sunada (1990) to account for partial  
102 miscibility of phases, so as to study the control of capillary pressure on salt precipitation  
103 during CO<sub>2</sub> injection in saline formations.

104 The outline of this article is as follows. First, a PDE to describe partially miscible  
105 three phase flow is presented. This is then reduced to an ordinary differential equation  
106 (ODE) by application of a similarity transform. The resulting boundary value problem  
107 is solved using a Chebyshev polynomial differentiation matrix. The necessary equations  
108 are then presented to determine the volume fraction of precipitated salt in the dry-out  
109 zone. A set of verification examples are presented based on a gas-displacing-oil scenario,  
110 previously presented by Orr (2007). A CO<sub>2</sub>-injection-in-a-saline-formation scenario is  
111 then presented, which is compared with simulation results from TOUGH2 for verification.  
112 Finally, a wider sensitivity analysis is conducted to better understand the main controls  
113 in this context.

## 114 2. Mathematical model

115 A homogenous, cylindrical and porous saline formation is invoked with a thickness  
116 of  $H$  [L] and an infinite radial extent. The pore space is initially fully saturated with  
117 a brine of uniform NaCl concentration. Pure CO<sub>2</sub> is injected at a constant rate of  $Q_0$   
118 [L<sup>3</sup>T<sup>-1</sup>] into the center of the saline formation via a fully penetrating injection well  
119 of infinitesimally small radius. The permeability of the saline formation is horizontally

120 isotropic. However, a necessary simplifying assumption is that the vertical permeability  
 121 is significantly smaller than the horizontal permeability such that gravity effects can be  
 122 neglected. In this way, during the injection phase, fluid flow can be treated as a one-  
 123 dimensional radially symmetric process.

124 Now we will describe the material mixture that resides within the pore-space. Consider  
 125 a mixture of three components:  $i = 1, 2$  and 3. Components 1 and 2 are mutually soluble  
 126 and can reside within both a non-wetting fluid phase and a wetting fluid phase, denoted  
 127 hereafter as  $j = 1$  and 2, respectively. Component 3 can dissolve into phase 2 and  
 128 precipitate to form a solid phase, denoted hereafter as  $j = 3$ . However, component 3 is  
 129 assumed not to be able to reside in phase 1 and components 1 and 2 are assumed not to  
 130 be able to reside in phase 3. In the context of a CO<sub>2</sub>-H<sub>2</sub>O-NaCl system,  $i = 1, 2$  and 3  
 131 for CO<sub>2</sub>, H<sub>2</sub>O and NaCl, respectively. All components are assumed to be incompressible  
 132 and not to experience volume change on mixing, such that component densities can be  
 133 treated as constant throughout.

134 The volume fraction of component  $i$  for the combined mixture,  $C_i$  [-], is defined by

$$C_i = \sum_{j=1}^3 \sigma_{ij} S_j \quad (2.1)$$

135 where  $\sigma_{ij}$  [-] is the volume fraction of component  $i$  in phase  $j$  and  $S_j$  [-] is the volume  
 136 fraction of phase  $j$  for the combined mixture, often referred to as the saturation of  
 137 phase  $j$ .

138 With no additional assumptions, it can be said that

$$\sum_{i=1}^3 C_i = \sum_{i=1}^3 \sigma_{ij} = \sum_{j=1}^3 S_j = 1 \quad (2.2)$$

139 and

$$\sigma_{ij} = \begin{cases} C_i, & C_1 \notin (c_{12}(1 - S_3), c_{11}(1 - S_3)), \quad i \in \{1, 2\}, \quad j \in \{1, 2\} \\ c_{ij}, & C_1 \in (c_{12}(1 - S_3), c_{11}(1 - S_3)), \quad i \in \{1, 2\}, \quad j \in \{1, 2\} \\ 0, & C_1 \in [0, 1], \quad i \in \{1, 2\}, \quad j = 3 \\ 0, & C_3 \in [0, 1], \quad i = 3, \quad j = 1 \\ C_3/S_2, & C_3 \in [0, c_{32}S_2], \quad i = 3, \quad j = 2 \\ c_{32}, & C_3 \in [c_{32}S_2, 1], \quad i = 3, \quad j = 2 \\ 1, & C_3 \in [0, 1], \quad i = 3, \quad j = 3 \end{cases} \quad (2.3)$$

140 where  $c_{ij}$  [-] is the constant equilibrium volume fraction of component  $i$  in phase  $j$ . It

141 further follows that

$$S_1 = \begin{cases} 0, & C_1 \leq c_{12}(1 - S_3) \\ \frac{C_1 - c_{12}(1 - S_3)}{c_{11} - c_{12}}, & c_{12}(1 - S_3) < C_1 < c_{11}(1 - S_3) \\ 1 - S_3, & C_1 \geq c_{11}(1 - S_3) \end{cases} \quad (2.4)$$

142 and

$$S_3 = \begin{cases} 0, & 0 \leq C_1 \leq 1, & C_3 < c_{32}S_2 \\ \frac{C_3 - c_{32}}{1 - c_{32}}, & C_1 \leq c_{12}(1 - S_3), & C_3 \geq c_{32}S_2 \\ \frac{(c_{11} - c_{12})C_3 - (c_{11} - C_1)c_{32}}{(1 - c_{32})c_{11} - c_{12}}, & c_{12}(1 - S_3) < C_1 < c_{11}(1 - S_3), & C_3 \geq c_{32}S_2 \\ C_3, & C_1 \geq c_{11}(1 - S_3), & C_3 \geq c_{32}S_2 \end{cases} \quad (2.5)$$

143 Under the above set of assumptions, fluid flow is controlled by the following set of

144 one-dimensional radially symmetric mass conservation equations

$$\phi \frac{\partial C_i}{\partial t} = -\frac{1}{r} \frac{\partial}{\partial r} \left( r \sum_{j=1}^2 q_j \sigma_{ij} \right), \quad i \in \{1, 2, 3\} \quad (2.6)$$

145 where  $\phi$  [-] is the saline formation porosity,  $t$  [T] is time,  $r$  [L] is radial distance from the

146 injection well and  $q_j$  [LT<sup>-1</sup>] is the flow of phase  $j$  per unit area, which can be found from

147 Darcy's law

$$q_j = -\frac{kk_{rj}}{\mu_j} \frac{\partial P_j}{\partial r}, \quad j \in \{1, 2\} \quad (2.7)$$

148 where  $k$  [ $L^2$ ] is the saline formation permeability and  $k_{rj}$  [-],  $\mu_j$  [ $ML^{-1}T^{-1}$ ] and  $P_j$   
 149 [ $ML^{-1}T^{-2}$ ] are the relative permeability, dynamic viscosity and pressure of phase  $j$ ,  
 150 respectively.

151 A detailed discussion with regards to justification for the above set of assumptions is  
 152 provided in Section 4 below.

153 The difference between the non-wetting and wetting phase pressure is referred to as  
 154 the capillary pressure,  $P_c$  [ $ML^{-1}T^{-2}$ ], i.e.,

$$P_c = P_1 - P_2 \quad (2.8)$$

155 Because the component densities are assumed to be constant, the system of equations  
 156 is divergence free and

$$\sum_{j=1}^2 q_j = \frac{Q_0}{2\pi Hr} \quad (2.9)$$

157 Substituting Eqs. (2.7) and (2.8) into Eq. (2.9), solving for the partial derivatives of  
 158  $P_j$  and then substituting these back into Eq. (2.7) leads to

$$q_j = \frac{Q_0 f_j}{2\pi Hr} + \frac{(-1)^j k k_{r1} f_2}{\mu_1} \frac{\partial P_c}{\partial r} \quad (2.10)$$

159 where, with further consideration of Eq. (2.4),

$$f_j = \begin{cases} [1 + (-1)^j] / 2, & C_1 \leq c_{12}(1 - S_3) \\ \frac{k_{rj}}{\mu_j} \left( \sum_{j=1}^2 \frac{k_{rj}}{\mu_j} \right)^{-1}, & c_{12}(1 - S_3) < C_1 < c_{11}(1 - S_3) \\ [1 + (-1)^{j-1}] / 2, & C_1 \geq c_{11}(1 - S_3) \end{cases} \quad (2.11)$$

160 Also note that there is no capillary pressure gradient when only one fluid phase is  
 161 present, i.e.,

$$\frac{\partial P_c}{\partial r} = 0, \quad C_1 \notin (c_{12}(1 - S_3), c_{11}(1 - S_3)) \quad (2.12)$$

162 Substituting Eq. (2.10) into Eq. (2.6), therefore leads to

$$\frac{\partial C_i}{\partial \tau} = -\frac{\partial F_i}{\partial \xi} \quad (2.13)$$

163 where

$$F_i = \begin{cases} \sigma_{i2}, & C_1 \leq c_{12}(1 - S_3) \\ \sum_{j=1}^2 f_j \sigma_{ij} + \left( \frac{k_{r1} f_2}{Ca} \sum_{j=1}^2 (-1)^j \sigma_{ij} \right) \xi \frac{\partial \psi}{\partial \xi}, & c_{12}(1 - S_3) < C_1 < c_{11}(1 - S_3) \\ \sigma_{i1}, & C_1 \geq c_{11}(1 - S_3) \end{cases} \quad (2.14)$$

164 and

$$\tau = \frac{Q_0 t}{\pi \phi H r_e^2} \quad (2.15)$$

165

$$\xi = \frac{r^2}{r_e^2} \quad (2.16)$$

166

$$\psi = \frac{P_c}{P_{c0}} \quad (2.17)$$

167 where  $r_e$  [L] is an arbitrary reference length,  $P_{c0}$  [ $\text{ML}^{-1}\text{T}^{-2}$ ] is a reference “air-entry”  
 168 pressure for the porous medium of concern and  $Ca$  [-] is a dimensionless constant often  
 169 referred to as the capillary number, found from

$$Ca = \frac{Q_0 \mu_1}{4\pi H k P_{c0}} \quad (2.18)$$

170 The capillary number represents the ratio of the  $\text{CO}_2$  injection rate to the product of  
 171 the  $\text{CO}_2$  mobility and air-entry pressure of the porous medium. It compares the relative  
 172 effect of the frictional resistance associated with fluid movement with the surface tension,  
 173 which acts across the interface between the  $\text{CO}_2$ -rich phase and the aqueous phase. Small  
 174 values of  $Ca$  imply that capillary processes are important.

175 With regards to the initial condition and boundary conditions, let  $C_{iI}$  [-] represent  
 176 a uniform initial value of  $C_i$  in the saline formation and  $C_{i0}$  [-] represent a constant  
 177 boundary value of  $C_i$  at the injection well for  $i \in \{1, 2, 3\}$ .

178

2.1. Writing capillary pressure in terms of  $C_1$ 

179 As  $\text{CO}_2$  is injected into the saline formation,  $\text{H}_2\text{O}$  evaporates from the brine leaving  
 180  $\text{NaCl}$  behind as a precipitate in a dry-out zone that develops around the injection well.  
 181 Following the commencement of  $\text{CO}_2$  injection, there are therefore three distinct zones  
 182 within the saline formation that should be considered (see Fig. 1): (1) The dry-out zone,  
 183 which surrounds the injection well and contains only precipitated salt and  $\text{CO}_2$  in the  
 184 non-wetting fluid phase. (2) The full mixture zone, which surrounds the dry-out zone  
 185 and contains  $\text{CO}_2$ ,  $\text{H}_2\text{O}$  and  $\text{NaCl}$ , distributed between the wetting and non-wetting  
 186 fluid phases. (3) The initial saline formation fluid zone, which surrounds the full mixture  
 187 zone and contains only  $\text{H}_2\text{O}$  and  $\text{NaCl}$  in a wetting fluid phase.

188 Inspection of Eqs. (2.13) and (2.14) reveals that the problem is hyperbolic for  $C_1 \notin$   
 189  $(c_{12}(1 - S_3), c_{11}(1 - S_3))$  and not hyperbolic for  $C_1 \in (c_{12}(1 - S_3), c_{11}(1 - S_3))$ , because of  
 190 the  $\partial\psi/\partial\xi$  term. For the  $\text{CO}_2$  injection scenario described above, both Zones 1 and 3 are  
 191 hyperbolic. In contrast, Zone 2 is not hyperbolic. The discontinuities that separate the  
 192 three zones are shock waves, which must satisfy the Rankine-Hugoniot condition (e.g.  
 193 Orr 2007).

194 Within Zone 2, the displacement of a wetting phase by a non-wetting phase represents  
 195 a continuous drainage cycle such that  $\psi$  can be treated as a unique function of  $S_2$ .  
 196 Furthermore, because  $S_3 = 0$  and  $S_2 = 1 - S_1$ , it follows, from Eq. (2.4), that

$$S_2 = \begin{cases} 1, & C_1 \leq c_{12} \\ \frac{c_{11} - C_1}{c_{11} - c_{12}}, & c_{12} < C_1 < c_{11} \\ 0, & C_1 \geq c_{11} \end{cases} \quad (2.19)$$

197 and

$$\frac{\partial S_2}{\partial C_1} = \frac{1}{(c_{12} - c_{11})}, \quad C_1 \in (c_{12}, c_{11}) \quad (2.20)$$

198 such that it can be said that

$$\frac{\partial \psi}{\partial \xi} = \frac{1}{(c_{12} - c_{11})} \frac{\partial \psi}{\partial S_2} \frac{\partial C_1}{\partial \xi} \quad (2.21)$$

199 In this way, Eq. (2.14) can be substantially simplified to get

$$F_i = \alpha_i - \beta_i \xi \frac{\partial C_1}{\partial \xi} \quad (2.22)$$

200 where

$$\alpha_i = \begin{cases} C_i, & C_1 \notin (c_{12}, c_{11}), \quad i \in \{1, 2\} \\ \sum_{j=1}^2 f_j c_{ij}, & C_1 \in (c_{12}, c_{11}), \quad i \in \{1, 2\} \\ f_2 \sigma_{32}, & C_1 \in [0, 1], \quad i = 3 \end{cases} \quad (2.23)$$

201

$$\beta_i = \begin{cases} 0, & C_1 \notin (c_{12}, c_{11}), \quad i \in \{1, 2, 3\} \\ G \sum_{j=1}^2 (-1)^j c_{ij}, & C_1 \in (c_{12}, c_{11}), \quad i \in \{1, 2\} \\ G \sigma_{32}, & C_1 \in (c_{12}, c_{11}), \quad i = 3 \end{cases} \quad (2.24)$$

202 and

$$G = \frac{f_2 k_{r1}}{\text{Ca}(c_{11} - c_{12})} \frac{\partial \psi}{\partial S_2} \quad (2.25)$$

203 When  $\text{Ca} \rightarrow \infty$  and  $\sigma_{32} = 0$ , the above problem reduces to the hyperbolic problem  
 204 solved by Orr (2007) using the MOC. When  $c_{11} = 1$ ,  $c_{12} = 0$  and  $\sigma_{32} = 0$ , the above  
 205 problem reduces to the immiscible two-phase flow problem with capillary pressure, pre-  
 206 viously solved by McWhorter and Sunada (1990) and Bjornara and Mathias (2013). The  
 207  $G$  term in Eq. (2.25) is analogous to the  $G$  term in Eq. (16) of Bjornara and Mathias  
 208 (2013).

## 2.2. Relative permeability and capillary pressure functions

210 Relative permeability is calculated from Corey curves but with relative permeability  
 211 assumed to linearly increase with saturation to one beyond residual saturations:

$$k_{rj} = \begin{cases} 0, & S_j \leq S_{jc} \\ k_{rj0} \left( \frac{S_j - S_{jc}}{1 - S_{1c} - S_{2c}} \right)^{n_j}, & S_{jc} < S_j < 1 - S_{ic} \quad , \quad i \neq j \\ k_{rj0} + (1 - k_{rj0}) \left( \frac{S_j - 1 + S_{ic}}{S_{ic}} \right), & S_j \geq 1 - S_{ic} \end{cases} \quad (2.26)$$

212 Dimensionless capillary pressure,  $\psi$ , is calculated using the empirical equation of van  
 213 Genuchten (1980) in conjunction with, following Oostrom *et al.* (2016) and Zhang *et al.*  
 214 (2016), the dry-region extension of Webb (2000):

$$\psi = \begin{cases} (S_e^{-1/m} - 1)^{1/n}, & S_2 > S_{2m} \\ \psi_d \exp \left[ \ln \left( \frac{\psi_m}{\psi_d} \right) \frac{S_2}{S_{2m}} \right], & S_2 \leq S_{2m} \end{cases} \quad (2.27)$$

215 where  $S_e$  [-] is an effective saturation found from

$$S_e = \frac{S_2 - S_{2c}}{1 - S_{2c}} \quad (2.28)$$

216 and  $k_{rj0}$  [-],  $S_{jc}$  [-] and  $n_j$  [-] are the end-point relative permeability, residual saturation  
 217 and relative permeability exponent for phase  $j$ , respectively,  $m$  [-] and  $n$  [-] are empir-  
 218 ical exponents associated with van Genuchten's function,  $\psi_d = P_{cd}/P_{c0}$  [-] where  $P_{cd}$   
 219 [ML<sup>-1</sup>T<sup>-2</sup>] is the capillary pressure at which ‘‘oven-dry’’ conditions are said to have  
 220 occurred (according to Webb (2000), this is taken to be 10<sup>9</sup> Pa) with

$$S_{2m} = (1 - S_{2c})S_{em} + S_{2c} \quad (2.29)$$

221 and

$$\psi_m = (S_{em}^{-1/m} - 1)^{1/n} \quad (2.30)$$

222 where  $S_{em}$  [-] is a critical effective saturation at which the switch over between the  
 223 van Genuchten's function and Webb's extension take place, defined in the subsequent  
 224 sub-section.

225 Differentiation of (2.27) with respect to  $S_2$  leads to

$$\frac{\partial \psi}{\partial S_2} = \begin{cases} \frac{\psi}{(1 - S_{2c})mnS_e(S_e^{1/m} - 1)}, & S_2 > S_{2m} \\ \frac{\psi}{S_{2m}} \ln \left( \frac{\psi_m}{\psi_d} \right), & S_2 \leq S_{2m} \end{cases} \quad (2.31)$$

226 The van Genuchten capillary pressure function has been widely used in many previous  
 227 CO<sub>2</sub> injection studies (e.g. Pruess and Muller 2009; Kim *et al.* 2012; Mathias *et al.* 2013;  
 228 Oostrom *et al.* 2016; Zhang *et al.* 2016). The Corey relative permeability functions have  
 229 previously been useful in describing CO<sub>2</sub>-brine relative permeability data from at least  
 230 25 different experiments from the international literature (Mathias *et al.* 2013).

### 231 2.3. Determination of $S_{em}$

232 Considering Eq. (2.31), Webb (2000) defines  $S_{em}$  as the effective saturation at which

$$\frac{\psi_m}{(1 - S_{2c})mnS_{em}(S_{em}^{1/m} - 1)} = \frac{\psi_m}{S_{2m}} \ln \left( \frac{\psi_m}{\psi_d} \right) \quad (2.32)$$

233 Substituting Eqs. (2.30) and (2.29) into Eq. (2.32) and rearranging leads to

$$S_{em} = \frac{S_{em} + S_{2c}(1 - S_{2c})^{-1}}{mn(S_{em}^{1/m} - 1) \ln \left[ (S_{em}^{-1/m} - 1)^{1/n} \psi_d^{-1} \right]} \quad (2.33)$$

234 which must be solved iteratively. Webb (2000) suggests that four to five iterations are  
 235 sufficient. However, this will be strongly dependent on the initial estimate of  $S_{em0}$  applied.

236 For  $S_{2c} > 0$ , a good initial estimate of  $S_{em}$ ,  $S_{em0}$ , can be obtained by assuming  
 237  $S_{em0} \ll 1$  such that Eq. (2.33) reduces to

$$S_{em0} = \frac{S_{2c}(1 - S_{2c})^{-1}}{\ln [S_{em0} \psi_d^{nm}]} \quad (2.34)$$

238 which can be rearranged to get

$$W \exp(W) = z \quad (2.35)$$

239 where

$$z = \frac{S_{2c} \psi_d^{nm}}{(1 - S_{2c})} \quad (2.36)$$

240 and

$$W = \frac{S_{2c}}{(1 - S_{2c})S_{em0}} \quad (2.37)$$

241 Note that the functional inverse of  $z(W)$  in Eq. (2.35),  $W(z)$ , is given by the Lambert  
 242 W function. Furthermore, because  $z$  is always positive and real,  $W(z) = W_0(z)$ , otherwise  
 243 referred to as the zero branch, which has the following asymptotic expansion (Corless *et*  
 244 *al.* 1996)

$$W_0(z) = L_1 - L_2 + \frac{L_2}{L_1} + O\left(\left[\frac{L_2}{L_1}\right]^2\right) \quad (2.38)$$

245 where  $L_2 = \ln L_1$  and  $L_1 = \ln z$ .

246 In this way, it can be said that

$$S_{em0} = \frac{S_{2c}}{(1 - S_{2c})W_0(z)} \quad (2.39)$$

247 where  $z$  is found from Eq. (2.36).

248 Examples of the iterative calculation of  $S_{em}$  from initial guesses obtained from Eq.  
 249 (2.39) are presented in Table 1. When  $S_{2c} \leq 0.3$ , it can be seen that convergence is  
 250 achieved after just two iterations. When  $S_{2c} = 0.5$ , three iterations are required. When  
 251  $S_{2c} = 0.7$ , six iterations are required. The increase in the number of iterations required  
 252 with increasing  $S_{2c}$  is due to reducing validity of the  $S_{em} \ll 1$  assumption.

#### 253 2.4. Application of a similarity transform

254 The partial differential equation in Eq. (2.13) can be reduced to an ordinary differential  
 255 equation by application of the following similarity transform

$$\lambda = \frac{\xi}{\tau} \quad (2.40)$$

256 Substituting Eq. (2.40) into Eqs. (2.13) and (2.22) leads to

$$\frac{dF_i}{dC_i} = \lambda \quad (2.41)$$

TABLE 1. Examples of the iterative calculation of  $S_{em}$  for different values of  $S_{2c}$  (as indicated in the top row) using Eq. (2.33) with  $m = 0.5$ ,  $P_{c0} = 19.6$  kPa and  $P_{cd} = 10^9$  Pa. The initial guess,  $S_{em0}$ , is calculated using Eq. (2.39).

Iteration / $S_{2c}$	0.1	0.3	0.5	0.7
0	0.016496	0.054104	0.11525	0.2472
1	0.018951	0.061087	0.13012	0.29011
2	0.018927	0.061082	0.1305	0.29695
3	0.018927	0.061082	0.13051	0.29825
4	0.018927	0.061082	0.13051	0.29850
5	0.018927	0.061082	0.13051	0.29855
6	0.018927	0.061082	0.13051	0.29856
7	0.018927	0.061082	0.13051	0.29856

257 and

$$F_i = \alpha_i - \beta_i \lambda \frac{dC_1}{d\lambda} \quad (2.42)$$

258 Differentiating both sides of Eq. (2.41) with respect to  $C_i$  yields

$$\frac{d^2 F_i}{dC_i^2} = \frac{d\lambda}{dC_i} \quad (2.43)$$

259 which on substitution into Eq. (2.42), along with Eq. (2.41), and rearranging leads to

$$\frac{d^2 F_1}{dC_1^2} + \frac{\beta_1}{(F_1 - \alpha_1)} \frac{dF_1}{dC_1} = 0 \quad (2.44)$$

260 In the event that the boundary and initial values of  $C_1$ ,  $C_{10}$  and  $C_{1I}$ , respectively, are

261  $\notin (c_{12}, c_{11})$ , the boundary conditions for Eq. (2.44) must satisfy the Rankine-Hugoniot

262 conditions (similar to Orr 2007, p. 75):

$$\frac{dF_1}{dC_1} = \frac{\alpha_{10} - F_1}{C_{10} - C_1}, \quad C_1 \geq c_{11} \quad (2.45)$$

263

$$\frac{dF_1}{dC_1} = \frac{\alpha_{1I} - F_1}{C_{1I} - C_1}, \quad C_1 \leq c_{12} \quad (2.46)$$

264 where  $\alpha_{10}$  and  $\alpha_{1I}$  represent the boundary and initial values of  $\alpha_1$  associated with  $C_{10}$ 265 and  $C_{1I}$ , respectively. Alternatively, when  $C_{10}$  and  $C_{1I}$  are  $\in (c_{12}, c_{11})$ 

$$F_1 = \alpha_{10}, \quad C_1 = C_{10} \quad (2.47)$$

$$F_1 = \alpha_{1I}, \quad C_1 = C_{1I}$$

266 An efficient way of expressing both Eqs. (2.46) and (2.47) simultaneously is to state

267 instead:

$$\begin{aligned} (C_{10} - C_1) \frac{dF_1}{dC_1} + F_1 &= \alpha_{10}, \quad C_1 = \tilde{C}_{10} \\ (C_{1I} - C_1) \frac{dF_1}{dC_1} + F_1 &= \alpha_{1I}, \quad C_1 = \tilde{C}_{1I} \end{aligned} \quad (2.48)$$

268 where

$$\tilde{C}_{10} = H(C_{10} - c_{11})c_{11} + H(c_{11} - C_{10})C_{10} \quad (2.49)$$

269

$$\tilde{C}_{1I} = H(c_{12} - C_{1I})c_{12} + H(C_{1I} - c_{12})C_{1I} \quad (2.50)$$

270 and  $H(x)$  is a Heaviside function.

271

### 2.5. Pseudospectral solution

272 Following Bjornara and Mathias (2013), the boundary value problem described in the

273 previous section is solved using a Chebyshev polynomial differentiation matrix,  $\mathbf{D}$  (Wei-

274 deman and Reddy 2000).

275 The coordinate space for the Chebyshev nodes is  $x \in [-1, 1]$ . However, the solution276 space for  $F_1$  is  $C_1 \in [\tilde{C}_{1I}, \tilde{C}_{10}]$ . Therefore the Chebyshev nodes,  $\mathbf{x}_k$ , need to be mapped277 to the  $C_1$  space by the following transform

$$C_1 = \frac{\tilde{C}_{10} + \tilde{C}_{1I}}{2} + \left( \frac{\tilde{C}_{10} - \tilde{C}_{1I}}{2} \right) x \quad (2.51)$$

278 Consequently, it is necessary to introduce an appropriately transformed differentiation

279 matrix,  $\mathbf{E}$ , where

$$\mathbf{E} = \frac{dx}{dC_1} \mathbf{D} \quad (2.52)$$

280 and from Eq. (2.51)

$$\frac{dx}{dC_1} = \frac{2}{\tilde{C}_{10} - \tilde{C}_{1I}} \quad (2.53)$$

281 By applying the Chebyshev polynomial on the internal nodes and the Robin boundary  
282 conditions in Eq. (2.48) on the end nodes, Eq. (2.44) can be written in matrix form

283 (similar to Piche and Kannianen (2009) and Bjornara and Mathias (2013))

$$\mathbf{R}(\mathbf{F}) = \begin{bmatrix} \mathbf{E}_{2:N-1,:}^{(2)} \mathbf{F} + \mathbf{I}_{2:N-1,:} \text{diag} \left[ \frac{\beta_1}{F_1 - \alpha_1} \right] \mathbf{E}^{(1)} \mathbf{F} \\ (\mathbf{C}_N - C_{1I}) \mathbf{E}_{N,:}^{(1)} \mathbf{F} - \mathbf{I}_{N,:} \mathbf{F} + \alpha_{1I} \\ (\mathbf{C}_1 - C_{10}) \mathbf{E}_{1,:}^{(1)} \mathbf{F} - \mathbf{I}_{1,:} \mathbf{F} + \alpha_{10} \end{bmatrix} \quad (2.54)$$

284 where  $\mathbf{R}$  is the residual vector,  $\mathbf{F}$  is the solution vector for the dependent variable  $F_1$ ,

285  $\mathbf{C}$  is the vector containing the corresponding values of  $C_1$  and  $N$  denotes the number of

286 Chebyshev nodes to be solved for. The two last rows on the right-hand side of Eq. (2.54)

287 impose the Robin boundary conditions. Also note that  $\mathbf{E}^{(n)}$  can be obtained from  $\mathbf{E}^n$ .

288 The solution vector,  $\mathbf{F}$ , can be obtained by Newton iteration, whereby new iterations,

289  $\mathbf{F}_{(i+1)}$ , are obtained from

$$\mathbf{F}_{(i+1)} = \mathbf{F}_{(i)} - (\partial \mathbf{R} / \partial \mathbf{F}_{(i)})^{-1} \mathbf{R}(\mathbf{F}_{(i)}) \quad (2.55)$$

290 where  $\partial \mathbf{R} / \partial \mathbf{F}$  is the Jacobian matrix defined as

$$\frac{\partial \mathbf{R}}{\partial \mathbf{F}} = \begin{bmatrix} \mathbf{E}_{2:N-1,:}^{(2)} + \mathbf{I}_{2:N-1,:} \text{diag} \left[ \frac{\beta_1}{F_1 - \alpha_1} \right] \mathbf{E}^{(1)} - \mathbf{I}_{2:N-1,:} \text{diag} \left[ \text{diag} \left[ \frac{\beta_1}{(F_1 - \alpha_1)^2} \right] \mathbf{E}^{(1)} \mathbf{F} \right] \\ (\mathbf{C}_N - C_{1I}) \mathbf{E}_{N,:}^{(1)} - \mathbf{I}_{N,:} \\ (\mathbf{C}_1 - C_{10}) \mathbf{E}_{1,:}^{(1)} - \mathbf{I}_{1,:} \end{bmatrix} \quad (2.56)$$

291 Note that  $F_1$  is bounded by  $\alpha_1$  and  $\alpha_{10}$ . Therefore, a good initial guess is to set

292  $F_1 = \alpha_{10}$ . Following Bjornara and Mathias (2013), an additional correction step should

293 be applied in the Newton iteration to force the solution,  $F_1$ , to be less than  $\alpha_1$ . The  
 294 Newton iteration loop is assumed to have converged when the mean absolute value of  
 295  $\mathbf{R} \leq 10^{-9}$ . With 100 Chebyshev nodes (i.e.,  $N = 100$ ), convergence is typically achieved  
 296 with less than 200 iterations.

### 2.6. *Dealing with salt precipitation in the dry-out zone*

297  
 298 Now consider the case where pure CO<sub>2</sub> is injected into a porous medium (i.e.,  $\alpha_{10} = 1$ )  
 299 initially fully saturated with brine (i.e.,  $\alpha_{1I} = 0$ ). Let  $\sigma_{32}$  be the volume fraction of NaCl  
 300 in phase 2 throughout the system. In this way, the volume fraction of H<sub>2</sub>O in phase 2  
 301 prior to CO<sub>2</sub> injection is  $(1 - \sigma_{32})$ .

302 Let  $r_0$  [L] and  $r_I$  [L] be the radial extents of the dry-out zone and injected CO<sub>2</sub> plume  
 303 respectively. At any given time, the volume of H<sub>2</sub>O evaporated by the CO<sub>2</sub>,  $V_e$  [L<sup>3</sup>], can  
 304 be found from

$$V_e = 2\pi\phi H(1 - c_{11}) \int_{r_0}^{r_I} r S_1 dr \quad (2.57)$$

305 The volume of salt precipitated in the dry-out zone,  $V_s$  [L<sup>3</sup>], is found from

$$V_s = \frac{\sigma_{32} V_e}{1 - \sigma_{32}} \quad (2.58)$$

306 The volume of the dry-out zone where the salt is precipitated,  $V_d$  [L<sup>3</sup>], is found from

$$V_d = \pi\phi H r_0^2 \quad (2.59)$$

307 Another quantity of interest is the volume of CO<sub>2</sub> dissolved in the brine,  $V_c$  [L<sup>3</sup>], which  
 308 can be found from

$$V_c = 2\pi\phi H c_{12} \int_{r_0}^{r_I} r(1 - S_1) dr \quad (2.60)$$

309 Considering the definition of  $\lambda$  in Eq. (2.40) in conjunction with Eqs. (2.15) and (2.16)

$$r_0^2 = \frac{Q_0 t \lambda_0}{\pi\phi H} \quad \text{and} \quad r_I^2 = \frac{Q_0 t \lambda_I}{\pi\phi H} \quad (2.61)$$

310 where, recall Eqs. (2.41) and (2.48),  $\lambda_0$  and  $\lambda_I$  can be found from

$$\lambda_0 = \left. \frac{dF_1}{dC_1} \right|_{C_1=c_{11}} \quad \text{and} \quad \lambda_I = \left. \frac{dF_1}{dC_1} \right|_{C_1=c_{12}} \quad (2.62)$$

311 In this way it can be understood that:

$$V_e = (1 - c_{11})Q_0t \int_{\lambda_0}^{\lambda_I} S_1 d\lambda \quad (2.63)$$

312

$$V_d = Q_0t\lambda_0 \quad (2.64)$$

313

$$V_c = c_{12}Q_0t \int_{\lambda_0}^{\lambda_I} (1 - S_1) d\lambda \quad (2.65)$$

314 Noting that the rates at which  $V_s$  and  $V_d$  grow with time are constant it can also  
 315 be understood that the volume fraction of precipitated salt,  $C_3$ , will be both uniform  
 316 within the dry-out zone and constant with time. The value of  $C_3$  within the dry-out  
 317 zone, hereafter denoted as  $C_{30}$ , can be found from

$$C_{30} = \frac{(1 - c_{11})\sigma_{32}}{(1 - \sigma_{32})\lambda_0} \int_{\lambda_0}^{\lambda_I} S_1 d\lambda \quad (2.66)$$

318 Given that  $C_{10} = 1 - C_{30}$ ,  $C_{1I} = 0$ ,  $\alpha_{10} = 1$  and  $\alpha_{1I} = 0$ , the boundary conditions in  
 319 Eq. (2.48) reduce to

$$\begin{aligned} \frac{dF_1}{dC_1} &= \frac{1 - F_1}{1 - C_{30} - c_{11}}, & C_1 &= c_{11} \\ \frac{dF_1}{dC_1} &= \frac{F_1}{c_{12}}, & C_1 &= c_{12} \end{aligned} \quad (2.67)$$

320 Values of  $C_{30}$  can be obtained iteratively by repeating the procedures outlined in  
 321 Section 2.5 with successive estimates of  $C_{30}$  obtained from Eq. (2.66). Using an initial  
 322 guess of  $C_{30} = 0$ , this process is found to typically converge after less than 60 iterations.  
 323 The integrals in Eqs. (2.65) and (2.63) can be found by trapezoidal integration.

### 3. Sensitivity analysis

#### 3.1. Gas displacing oil

As a first example, the gas-displacing-oil scenario previously presented in Figs. 4.13 and 4.15 of Orr (2007) is adopted. The parameters describing the scenario include  $c_{11} = 0.95$ ,  $c_{12} = 0.20$ ,  $\sigma_{32} = 0$ ,  $\mu_2/\mu_1 = 2$ ,  $S_{1c} = 0.05$ ,  $S_{2c} = 0.1$ ,  $k_{r10} = k_{r20} = 1$  and  $n_1 = n_2 = 2$ . For the pseudospectral solution, a value for the van Genuchten (1980) parameter,  $m$ , is set to 0.5.

Plots of  $C_1$  against  $dF_1/dC_1$  (which, recall, is equal to  $\xi/\tau$ ) for this scenario are shown in Fig. 2. The different subplots show the effect of varying the boundary volume fraction,  $C_{10}$ , and the initial volume fraction,  $C_{1I}$ . The different colors relate to different assumed values of Ca. Increasing Ca can be thought of as analogous to an increased injection rate. The  $\text{Ca} \rightarrow \infty$  curves were obtained from the MOC solutions previously presented in Figs. 4.13 and 4.15 of Orr (2007). The finite Ca value solutions were obtained using the pseudospectral solution described above, with 100 Chebyshev nodes.

When  $\text{Ca} = 100$ , the pseudospectral solution is virtually identical to the infinite-Ca MOC solutions. As Ca is decreased, the solution becomes more diffused. In Figs. 2a, d, e and f, the infinity Ca results exhibit a trailing shock, which represents a dry-out zone where all the liquid oil has been evaporated by the gas. Of particular interest is that decreasing Ca leads to a reduction in the thickness of the dry-out zone, ultimately leading to its complete elimination.

#### 3.2. CO<sub>2</sub> injection in a saline formation

Here the CO<sub>2</sub>-injection-in-a-saline-formation scenario, previously presented by Mathias *et al.* (2013), is revisited. The example involves injecting pure CO<sub>2</sub> at a constant rate via a fully penetrating injection well at the center of a cylindrical, homogenous and confined

TABLE 2. Relevant model parameters used for the CO<sub>2</sub> injection in saline formation scenario, previously presented by Mathias *et al.* (2013).

CO <sub>2</sub> injection rate,	15 kg s <sup>-1</sup>
Porosity, $\phi$	0.2
Initial pressure	10 MPa
Temperature	40 °C
Mass fraction of salt in brine, $X_{32}$	0.15
Critical gas saturation, $S_{1c}$	0.0
Residual water saturation, $S_{2c}$	0.5
End-point relative permeability for CO <sub>2</sub> , $k_{r10}$	0.3
End-point relative permeability for brine, $k_{r20}$	1.0
Relative permeability exponents, $n_1, n_2$	3
Formation thickness, $H$	30 m
Permeability, $k$	10 <sup>-13</sup> m <sup>2</sup>

348 saline formation, initially fully saturated with brine. Relevant model parameters are  
 349 presented in Table 2. In this case, components 1, 2 and 3 are CO<sub>2</sub>, H<sub>2</sub>O and NaCl,  
 350 respectively, and phases 1, 2 and 3 represent a CO<sub>2</sub>-rich phase, an H<sub>2</sub>O rich phase and  
 351 precipitated salt, respectively.

352 The relevant fluid properties are obtained using equations of state (EOS) and empirical  
 353 equations provided by Batzle and Wang (1992), Fenghour *et al.* (1998), Spycher *et al.*  
 354 (2003) and Spycher and Pruess (2005). Mathias *et al.* (2011a) found that when using  
 355 analytical solutions in this context, to account for the relatively high compressibility  
 356 of CO<sub>2</sub>, it is important to use an estimate of the final pressure rather than the initial  
 357 pressure for calculating the fluid properties relating to CO<sub>2</sub>. Mathias *et al.* (2013) found  
 358 that, for the scenario described in Table 2, the well pressure increased by just over 5 MPa

359 after ten years. Therefore, for the current study, fluid properties are calculated using 15  
 360 MPa as opposed to 10 MPa.

361 The EOS of Spycher *et al.* (2003) and Spycher and Pruess (2005) provide equilibrium  
 362 mole fractions as opposed to volume fractions. Pruess and Spycher (2007) show how mole  
 363 fractions can be converted to mass fractions,  $x_{ij}$  [-], which can be converted to volume  
 364 fractions,  $\sigma_{ij}$  [-], using (similar to Orr 2007, p. 19)

$$\sigma_{ij} = \frac{\rho_j x_{ij}}{\rho_{ij}} \quad (3.1)$$

365 where  $\rho_{ij}$  [ $\text{ML}^{-3}$ ] is the density of component  $i$  in phase  $j$  and  $\rho_j$  [ $\text{ML}^{-3}$ ] is the composite  
 366 phase density, which can be found from

$$\rho_j = \left( \sum_{i=1}^{N_c} \frac{x_{ij}}{\rho_{ij}} \right)^{-1} \quad (3.2)$$

367 where  $N_c$  [-] is the number of components present. Because the pseudospectral solution  
 368 above assumes component densities remain constant throughout, a decision is made that  
 369  $\rho_{12} = \rho_{11}$ ,  $\rho_{21} = \rho_{22}$  and  $\rho_{32} = \rho_{33}$ .

370 Table 3 shows how the various fluid properties vary with depth below sea-level in this  
 371 context. Depth is related to pressure by assuming hydrostatic conditions and then adding  
 372 5 MPa to allow for pressure induced by  $\text{CO}_2$  injection. Depth is related to temperature  
 373 by assuming a geothermal gradient of  $40^\circ\text{C}$  per km. It can be seen that the volume  
 374 fractions are largely unaffected by depth. However, the variation in brine viscosity and  
 375  $\text{CO}_2$  density are more noticeable.

376 A comparison of results from the pseudospectral solution with those from the TOUGH2  
 377 simulation reported by Mathias *et al.* (2013) is shown in Fig. 3, alongside results for when  
 378  $\text{Ca} \rightarrow \infty$ , obtained using a MOC solution similar to that previously presented by Zeidouni  
 379 *et al.* (2009) and Mathias *et al.* (2011b). Mathias *et al.* (2013) assumed  $P_{c0} = 19.6$  kPa.  
 380 Considering the other parameters in Tables 2 and 3, this leads to a Ca value of 1.7.

TABLE 3. Relevant model parameters used for the CO<sub>2</sub> injection in a saline formation scenario with a brine salinity of 150 ppt.

Depth (m)	1000	1500	2000
Pressure (MPa)	15	20	25
Temperature (°C)	40	60	80
Density of CO <sub>2</sub> , $\rho_{11}$ (kg m <sup>-3</sup> )	754	704	673
Density of H <sub>2</sub> O, $\rho_{22}$ (kg m <sup>-3</sup> )	998	992	984
Density of NaCl, $\rho_{33}$ (kg m <sup>-3</sup> )	2160	2160	2160
Volume fraction of CO <sub>2</sub> in phase 1, $c_{11}$ (-)	0.999	0.998	0.996
Volume fraction of CO <sub>2</sub> in phase 2, $c_{12}$ (-)	0.041	0.043	0.045
Volume fraction of NaCl in phase 2, $\sigma_{32}$ (-)	0.075	0.074	0.073
Dynamic viscosity of CO <sub>2</sub> , $\mu_1$ (cP)	0.064	0.057	0.054
Dynamic viscosity of brine, $\mu_2$ (cP)	0.963	0.730	0.573

381 There is excellent correspondence between the MOC solution, the TOUGH2 results and  
 382 the pseudospectral solution when  $Ca = 1.7$ .

383 A value of  $P_{c0} = 19.6$  kPa is often used to describe saline formations in a CO<sub>2</sub> storage  
 384 context (Rutqvist *et al.* 2007; Zhou *et al.* 2008; Mathias *et al.* 2013; Zhu *et al.* 2015, e.g.).  
 385 Experimental analysis looking at four different sandstone reservoirs revealed a range of  
 386  $P_{c0}$  values from 1.3 to 7.1 kPa (Oostrom *et al.* 2016). Smaller values of  $P_{c0}$  imply larger  
 387 pore diameters.

388 A hallmark of hyperbolic theory is that the problem can be reduced to a fundamental  
 389 wave structure which constitutes the solution. In Fig. 3, it can be seen that such a wave  
 390 structure is largely preserved, despite the inclusion of capillary diffusion. Furthermore,  
 391 the wave velocity of the leading shock is virtually independent of  $Ca$  for the range of  $Ca$

values studied. However, decreasing  $Ca$  leads to a more diffused spreading wave caused by the increase in capillary diffusion, which in turn leads to a reduction in the wave velocity of the trailing shock, as also seen in Fig. 2a. The decrease in steady-state  $CO_2$  saturation in the dry-out zone is caused by an increase in the volume fraction of precipitated salt (recall that  $C_{10} = 1 - C_{30}$ ).

For the scenarios depicted in Fig. 3,  $C_{30}$  is found to be insensitive to  $Ca$  for  $Ca$  values greater than or equal to 1.7. However for  $Ca$  values less than 1.7, the volume of the dry-out zone is significantly reduced and the volume fraction of precipitated salt is significantly increased. The value of  $C_{30}$  for  $Ca = 0.2$  is almost double the value for  $Ca = 1.7$ . The value of  $C_{30}$  for  $Ca = 0.1$  is around ten times that of when  $Ca = 1.7$ . The  $Ca = 1.7$  scenario described in Table 2 assumes an injection rate of  $15 \text{ kg s}^{-1}$ . The results shown in Fig. 3 therefore suggest that reducing the injection rate down to  $1.8 \text{ kg s}^{-1}$  would lead to a doubling of the volume fraction of precipitated salt around the injection well. Furthermore, reducing the injection rate from  $15 \text{ kg s}^{-1}$  down to  $0.9 \text{ kg s}^{-1}$  would lead to an almost ten times larger volume fraction of precipitated salt around the injection well.

For the hyperbolic case when  $Ca \rightarrow \infty$ , it is common to study plots of  $F_1$  and  $C_1$  (Orr 2007). Fig. 4a shows plots of  $F_1$  against  $C_1$  for all the values of  $Ca$  presented in Fig. 3 along with a plot of  $\alpha_1$ . The MOC solution (i.e., with  $Ca \rightarrow \infty$ ), which sits almost exactly underneath the  $Ca = 1.7$  line, intersects the  $\alpha_1$  line at tangents, which is symptomatic of satisfying the shock waves satisfying the Rankine-Hugoniot condition. To better visualize the results for finite  $Ca$  values,  $(1 - F_1)$  is shown on a log-scale in Fig. 4b. Here it can be seen that the models approach a value of  $F_1 = 1$  at different  $C_1$  values depending on the volume fraction of precipitated salt. The volume fraction of precipitated salt increases with decreasing  $Ca$ . Fig. 4c shows a close-up view of the trailing shocks on linear axes

417 for further reference. For finite Ca values, the  $F_1$  lines never actually intersect the  $\alpha_1$   
418 line except at where  $C_1 = 0$ . The reason for this is due to  $\beta_1$ , which is plotted in Fig.  
419 4d. The highest values of  $\beta_1$  are at the center of the two-phase region,  $C_1 \in (c_{12}, c_{11})$ .  $\beta_1$   
420 smoothly grades down to zero as it reaches the single-phase regions,  $C_1 \notin (c_{12}, c_{11})$ .

421 A further sensitivity analysis is presented in Fig. 5. The three depth scenarios presented  
422 in Table 3 are applied with three different brine salinities. Fig. 5a shows how the volume  
423 of the dry-out zone decreases with decreasing Ca. The size of the dry-out zone increases  
424 with increasing depth. In contrast, brine salinity has very little impact on dry-out zone  
425 volume.

426 Fig. 5b shows the volume of the evaporated water also reduces with decreasing Ca. At  
427 first this seems surprising given that capillary pressure effects should bring more water  
428 into the dry-out zone. However, the effect of the capillary pressure is also to spread the  
429  $\text{CO}_2$  out further (see leading edge of  $\text{CO}_2$  plumes in Fig. 3). As a consequence, more  $\text{CO}_2$   
430 is dissolved (see Fig. 5c). Consequently, less of the  $\text{CO}_2$ -rich phase is available for water  
431 from the brine to evaporate into. The volume of evaporated water increases with depth  
432 because the equilibrium volume fraction of water in the  $\text{CO}_2$ -rich phase increases with  
433 depth (see Table 3). The volume of dissolved  $\text{CO}_2$  is insensitive to depth but decreases  
434 with increasing brine salinity. The latter is because the solubility limit of  $\text{CO}_2$  in brine  
435 decreases substantially with increasing salinity (Spycher and Pruess 2005).

436 Fig. 5d shows how volume fraction of precipitated salt in the dry-out zone,  $C_{30}$ , super-  
437 linearly increases with decreasing Ca. For  $\text{Ca} > 0.25$ , the quantity of precipitated salt is  
438 mostly controlled by brine salinity. However, for  $\text{Ca} < 0.25$ , depth plays an increasingly  
439 important role, with higher levels of salt precipitation in shallower formations. This is  
440 because the dry-out zone increases with depth, despite increasing water evaporation with  
441 depth. Fig. 6 shows the same results as Fig. 5d but with  $C_{30}$  normalized by dividing by

442 the salinity of the brine,  $X_{32}$ . Here it can be seen that  $C_{30}$  almost linearly scales with  
443  $X_{32}$ .

444 The volume fraction of precipitated salt is also strongly controlled by the relative  
445 permeability parameters,  $k_{rj0}$ ,  $S_{jc}$  and  $n_j$  (Zhang *et al.* 2016). The analysis performed  
446 to provide Fig. 6 was repeated for the 1000 m depth scenario for each of the six groups  
447 of relative permeability parameters presented in Table 4. These six parameter sets were  
448 selected from a database of 25 core experiments previously compiled by Mathias *et al.*  
449 (2013). The six cores were selected to provide a representative range of possible outcomes,  
450 given the wide variability generally observed in such data sets.

451 From Fig. 7 it can be seen that the high Ca values of  $C_{30}$  range from 0.019 to 0.044.  
452 Furthermore, the critical Ca value below which  $C_{30}$  superlinearly increases ranges from  
453 0.025 to 10. Comparing these results with the parameter sets in Table 4 it can be seen  
454 that when the relative permeability for brine is more linear, the value of  $C_{30}$  at high values  
455 of Ca tends to be lower. However, this linearity also leads to the superlinearly increasing  
456 of  $C_{30}$  with decreasing Ca to occur at a relatively low value of  $C_{30}$  (see for example  
457 Cardium #1 and Basal Cambrian). Exactly the opposite happens when the relative  
458 permeability for brine is highly non-linear (see for example Paaratte and Tuscaloosa).  
459 This is probably due to counter-current flow of water being less efficient when relative  
460 permeability is highly non-linear.

## 461 4. Discussion of key modeling assumptions

### 462 4.1. Incompressible fluids

463 Fluid densities are assumed to be independent of pressure. The compressibilities of H<sub>2</sub>O  
464 and NaCl are commonly ignored. For pressures and temperatures associated with de-  
465pleted gas reservoirs, the compressibility of CO<sub>2</sub> is very high and has a significant impact

TABLE 4. Relative permeability parameters for six different sandstone cores (after Mathias *et al.* 2013). Note that for each core  $k_{r20} = 1$  and  $S_{1c} = 0$ . Data for Cardium #1, Basal Cambrian and Viking #1 was originally obtained by Bennion and Bachu (2008). Data for Otway was originally obtained by Perrin and Benson (2010). Data for Paaratte and Tuscaloosa was originally obtained by Krevor *et al.* (2012).

Unit	$k_{r10}$	$S_{2c}$	$n_1$	$n_2$
Cardium #1	0.526	0.197	1.7	1.3
Basal Cambrian	0.545	0.294	5.0	1.8
Otway	0.332	0.558	3.2	2.9
Viking #1	0.659	0.437	6.5	2.5
Paaratte	0.328	0.389	3.0	4.6
Tuscaloosa	0.077	0.703	3.2	4.7

466 on fluid movement (Mathias *et al.* 2014). However, for CO<sub>2</sub> injection in saline formations,  
 467 fluid pressures are expected to be hydrostatic or above. Under these conditions, providing  
 468 a sensible reference pressure is used to determine the fluid properties of CO<sub>2</sub> (i.e., an  
 469 estimate of pressure towards the end of the injection cycle), the compressibility of CO<sub>2</sub>  
 470 has been found to have a negligible effect in this context (Mathias *et al.* 2011a,b).

#### 471 4.2. No volume change on mixing

472 Component densities are assumed to be uniform across phases. In fact, the densities of  
 473 CO<sub>2</sub> and H<sub>2</sub>O are both higher in the aqueous phase as compared to in the CO<sub>2</sub>-rich phase.  
 474 For a wide range of different CO<sub>2</sub> injection scenarios, this volume change on mixing is  
 475 found to lead to an increase in volumetric flow rate of around 0.05% in Zone 2 and a

476 decrease in volumetric flow rate of around 5% in Zone 3 (see Table 2 of Mathias *et al.*  
477 2011b). See section 2.1 above for an explanation of the zone numbers.

478 With regards to NaCl, the density of precipitated NaCl,  $\rho_{33}$ , is 2160 kg m<sup>-3</sup>. Using  
479 Eq. (3.2) in conjunction with the EOS for brine given by Batzle and Wang (1992), it can  
480 be shown that the density of NaCl dissolved in brine,  $\rho_{32}$ , is around 2800 kg m<sup>-3</sup>. In the  
481 above analysis we have set  $\rho_{32} = \rho_{33}$  such that the model precipitates the correct volume  
482 of salt in the dry-out zone. The consequence is that the volume fractions of water and  
483 CO<sub>2</sub> in the brine are underestimated by around 2%.

484 Fig. 3 compares model results from TOUGH2 with those from the similarity solution.  
485 TOUGH2 properly incorporates fluid compressibility and volume change on mixing and  
486 there is negligible difference between the two models.

#### 487 4.3. Ignoring gravity effects

488 As stated earlier, another important assumption is that the vertical permeability of  
489 the formation is sufficiently low that gravity effects can be ignored. Extreme changes  
490 in density and/or viscosity can lead to instabilities and fingering phenomena, which  
491 cannot be represented using one-dimensional models. Indeed, Kim *et al.* (2012) found  
492 that buoyancy driven flow, associated with the different densities of brine and CO<sub>2</sub>,  
493 played an important part in controlling the spatial distribution of precipitated salt around  
494 an injection well. However, this was mostly after the cessation of injection. During the  
495 injection phase, gravity segregation within the dry-out zone was much less significant  
496 and no viscous fingering was observed.

497 Mathias *et al.* (2011b) presented a comparison of simulation results where gravity  
498 was accounted for and ignored using TOUGH2 and the MOC solution of Zeidouni *et*  
499 *al.* (2009), respectively. For a 100 m thick isotropic saline formation, gravity was found  
500 to have a strong effect on the leading edge of the CO<sub>2</sub> plume. However, gravity effects

501 were found to be negligible on the dry-out zone development and the associated volume  
 502 fraction of the precipitated salt. For a 50 m thick isotropic saline formation, gravity  
 503 effects were found to be negligible throughout.

504 The dry-out zone is generally unaffected by gravity segregation due to the larger ve-  
 505 locities situated close around the injection well, which are mostly horizontal due to the  
 506 horizontal driving force provided by the injection well boundary (Mathias *et al.* 2011b).  
 507 From the discussion above it is expected that gravity effects are unlikely to significantly  
 508 affect the dry-out zone in the 30 m thick saline formations studied in this current article,  
 509 at least for the lower capillary numbers studied. However, as the capillary numbers are  
 510 increased, the horizontal injection velocities will become less significant and gravity will  
 511 play a more important role. However, our analysis has shown that excessive salt pre-  
 512 cipitation can also develop in the absence of gravity effects due to the counter-current  
 513 imbibition associated with capillary pressure.

## 514 5. Summary and conclusions

515 A new similarity solution has been presented to study the role of capillary pressure  
 516 on salt precipitation during CO<sub>2</sub> injection in a saline formation. Dimensional analy-  
 517 sis has revealed that the problem is largely controlled by a capillary number,  $Ca =$   
 518  $Q_0\mu_1/(4\pi HkP_{c0})$ , where  $H$  [L] is the formation thickness,  $k$  [L<sup>2</sup>] is permeability,  $P_{c0}$   
 519 [ML<sup>-1</sup>T<sup>-2</sup>] is an air-entry pressure associated with the porous medium,  $Q_0$  [L<sup>3</sup>T<sup>-1</sup>]  
 520 is the injection rate and  $\mu_1$  [ML<sup>-1</sup>T<sup>-1</sup>] is the dynamic viscosity of CO<sub>2</sub>. The volume  
 521 fraction of precipitated salt around the injection well,  $C_{30}$  [-], is found to superlinearly  
 522 increase with decreasing  $Ca$ . Subsequent sensitivity analysis also reveals that  $C_{30}$  linearly  
 523 scales with the salinity of brine.  $C_{30}$  is found to reduce with increasing storage depth.  
 524 This latter point is largely attributed to the equilibrium volume fraction of water in

525 the CO<sub>2</sub>-rich phase increasing with depth. Relative permeability parameters are found  
526 to have a significant effect on the value of Ca below which  $C_{30}$  superlinearly increases.  
527 For highly non-linear relative permeabilities,  $C_{30}$  remains stable for much lower capillary  
528 numbers.

529 The new similarity solution represents a significant extension of the work of Zeidouni *et*  
530 *al.* (2009) by accounting for capillary pressure and an extension of the work of Bjornara  
531 and Mathias (2013) by accounting for radially symmetric flow, partial miscibility and  
532 salt precipitation.

533 In one scenario studied, reducing the CO<sub>2</sub> injection rate from 15 kg s<sup>-1</sup> to 0.9 kg  
534 s<sup>-1</sup> led to almost a ten times larger volume fraction of precipitated salt. In the past,  
535 pressure buildup in injection wells has been widely perceived to increase monotonically  
536 with CO<sub>2</sub> injection rate. However, these results clearly demonstrate that as injection  
537 rate is decreased the volume fraction of precipitated salt around the injection well will  
538 significantly increase leading to potentially significant loss of injectivity. It follows that  
539 below a critical threshold, pressure buildup can be expected to increase with reducing  
540 injection rates as well. The similarity solution presented in this article can serve as a  
541 useful tool to determine the critical capillary number at which these effects are likely to  
542 take place.

### 543 **Acknowledgements**

544 This work was funded by the Crown Estate.

### REFERENCES

- 545 BATZLE, M. & WANG, Z. 1992 Seismic properties of pore fluids, *Geophysics* **57**, 1396–1408.  
546 BENNION, B. & BACHU, S. 2008 Drainage and imbibition relative permeability relationships

- 547 for supercritical CO<sub>2</sub>/brine and H<sub>2</sub>S/brine systems in intergranular sandstone, carbonate,  
548 shale, and anhydrite rocks. *SPE Res. Eval. Eng.* **11**, 487–496.
- 549 BJORNARA, T. I. & MATHIAS, S. A. 2013 A pseudospectral approach to the McWhorter and  
550 Sunada equation for two-phase flow in porous media with capillary pressure. *Comp. Geosci.*  
551 **17**, 889–897.
- 552 CORLESS, R. M., GONNET, G. H., HARE, D. E., JEFFREY, D. J. & KNUTH, D. E. 1996 On  
553 the LambertW function, *Adv. Comput. Math.* **5**, 329–359.
- 554 FENGHOUR, A., WAKEHAM, W. A. & VESOVIC, V. 1998 The viscosity of carbon dioxide. *J.*  
555 *Phys. Chem. Ref. Data* **27**, 31–44.
- 556 FUCIK, R., MIKYSKA, J., BENES, M., & ILLANGASEKARE, T. H. 2007 An improved semi-  
557 analytical solution for verification of numerical models of two-phase flow in porous media.  
558 *Vadose Zone J.* **6**, 93–104.
- 559 HESSE, M. A., TCHELEPI, H. A., CANTWELL, B. J. & ORR JR, F. M. 2007 Gravity currents  
560 in horizontal porous layers: transition from early to late self-similarity. *J. Fluid Mech.* **577**,  
561 363–383.
- 562 HESSE, M. A., ORR, F. M. & TCHELEPI, H. A. 2008 Gravity currents with residual trapping.  
563 *J. Fluid Mech.* **611**, 35–60.
- 564 KIM, K. Y., HAN, W. S., OH, J., KIM, T. & KIM, J.-C. 2012 Characteristics of salt pre-  
565 cipitation and the associated pressure build-up during CO<sub>2</sub> storage in saline aquifers.  
566 *Transp. Porous Med.* **92**, 397–418.
- 567 KREVOR, S., PINI, R., ZUO, L. & BENSON, S. M. 2012 Relative permeability and trapping of  
568 CO<sub>2</sub> and water in sandstone rocks at reservoir conditions. *Water Resour. Res.* **48**, W02532.
- 569 LI, B., TCHELEPI, H. A. & BENSON, S. M. 2013 Influence of capillary-pressure models on CO<sub>2</sub>  
570 solubility trapping. *Adv. Water Resour.*, **62**, 488–498.
- 571 MACMINN, C. W., SZULCZEWSKI, M. L. & JUANES, R. 2010 CO<sub>2</sub> migration in saline aquifers.  
572 Part 1. Capillary trapping under slope and groundwater flow. *J. Fluid Mech.* **662**, 329–351.
- 573 MACMINN, C. W., SZULCZEWSKI, M. L. & JUANES, R. 2011 CO<sub>2</sub> migration in saline aquifers.  
574 Part 2. Capillary and solubility trapping. *J. Fluid Mech.* **688**, 321–351.
- 575 MATHIAS, S. A., GONZALEZ MARTINEZ DE MIGUEL, G. J., THATCHER, K. E., & ZIMMER-

- 576 MAN, R. W. 2009 Pressure buildup during CO<sub>2</sub> injection into a closed brine aquifer.  
577 *Transp. Porous Med.* **89**, 383–397.
- 578 MATHIAS, S. A., GLUYAS, J. G., GONZLEZ MARTNEZ DE MIGUEL, G. J. & HOSSEINI, S. A.  
579 2011 Role of partial miscibility on pressure buildup due to constant rate injection of CO<sub>2</sub>  
580 into closed and open brine aquifers. *Water Resour. Res.* **47**, W12525.
- 581 MATHIAS, S. A., GLUYAS, J. G., GONZLEZ MARTNEZ DE MIGUEL, G. J., BRYANT, S. L., &  
582 WILSON, D. 2013 On relative permeability data uncertainty and CO<sub>2</sub> injectivity estimation  
583 for brine aquifers. *Int. J. Greenh. Gas Control* **12**, 200–212.
- 584 MATHIAS, S. A., MCELWAIN, J. N. & GLUYAS, J. G. 2014 Heat transport and pressure buildup  
585 during carbon dioxide injection into depleted gas reservoirs. *J. Fluid Mech.* **756**, 89–109.
- 586 MCWHORTER, D. B. & SUNADA, D. K. 1990 Exact integral solutions for two-phase flow. *Water*  
587 *Resour. Res.* **26**, 399–413.
- 588 MIRI, R. & HELLEVANG, H. 2016 Salt precipitation during CO<sub>2</sub> storage—A review. *Int. J.*  
589 *Greenh. Gas Control* **51**, 136–147.
- 590 NORDBOTTEN, J. M. & CELIA, M. A. 2006 Similarity solutions for fluid injection into confined  
591 aquifers. *J. Fluid Mech.* **561**, 307–327.
- 592 OOSTROM, M., WHITE, M. D., PORSE, S. L., KREVER, S. C. M. & MATHIAS, S. A. 2016  
593 Comparison of relative permeability–saturation–capillary pressure models for simulation of  
594 reservoir CO<sub>2</sub> injection. *Int. J. Greenh. Gas Control* **45**, 70–85.
- 595 ORR JR., F. M. 2007 *Theory of Gas Injection Processes*, Tie-Line Publications, Denmark.
- 596 PERRIN, J. C. & BENSON, S. 2010 An experimental study on the influence of sub-core scale  
597 heterogeneities on CO<sub>2</sub> distribution in reservoir rocks. *Transp. Porous Med.* **82**, 93–109.
- 598 PICHE, R. & KANNIAINEN, J. 2009 Matrix-based numerical modelling of financial differential  
599 equations. *Int. J. Math. Model Numer. Optim.* **1**, 88–100.
- 600 PRUESS, K., & SPYCHER, N. 2007 ECO2Na fluid property module for the TOUGH2 code for  
601 studies of CO<sub>2</sub> storage in saline aquifers. *Energy Convers. and Manage.* **48**, 1761–1767.
- 602 PRUESS, K. & MULLER, N. 2009 Formation dry-out from CO<sub>2</sub> injection into saline aquifers. 1.  
603 Effects of solids precipitation and their mitigation. *Water Resour. Res.* **45**, W03402.
- 604 RUTQVIST, J., BIRKHOEHLER, J., CAPP, F. & TSANG, C. F. 2007 Estimating maximum sus-

- tainable injection pressure during geological sequestration of CO<sub>2</sub> using coupled fluid flow and geomechanical fault-slip analysis. *Energy Convers. and Manage.* **48**, 1798–1807.
- 605  
606
- 607 SPYCHER, N., PRUESS, K. & ENNIS-KING, J. 2003 CO<sub>2</sub>-H<sub>2</sub>O mixtures in the geological sequestration of CO<sub>2</sub>. I. Assessment and Calculation of Mutual Solubilities from 12 to 100 °C and up to 600 bar. *Geochim. Cosmochim. Acta* **67**, 3015–3031.
- 608  
609
- 610 SPYCHER, N. & PRUESS, K. 2005 CO<sub>2</sub>-H<sub>2</sub>O mixtures in the geological sequestration of CO<sub>2</sub>. II. Partitioning in chloride brines at 12–100 °C and up to 600 bar. *Geochim. Cosmochim. Acta* **69**, 3309–3320.
- 611  
612
- 613 VAN GENUCHTEN, M. T. 1980 A closed-form equation for predicting the hydraulic conductivity of unsaturated soils, *Soil Sci. Soc. Am. J.* **44**, 892–898.
- 614
- 615 WEBB, S. W. 2000 A simple extension of two-phase characteristic curves to include the dry region, *Water Resour. Res.* **36**, 1425–1430.
- 616
- 617 WEIDEMAN, J. A. C. & REDDY, S. C. 2000 A MATLAB differentiation matrix suite, *ACM Trans. Math. Softw.* **24**, 465–519.
- 618
- 619 ZEIDOUNI, M., POOLADI-DARVISH, M. & KEITH, D. 2009 Analytical solution to evaluate salt precipitation during CO<sub>2</sub> injection in saline aquifers. *Int. J. Greenh. Gas Control* **3**, 600–611.
- 620  
621
- 622 ZHANG, Z. F., OOSTROM, M. & WHITE, M. D. 2016 Relative permeability for multiphase flow for oven-dry to full saturation conditions. *Int. J. Greenh. Gas Control* **49**, 259–266.
- 623
- 624 ZHOU, Q., BIRKHOEHLER, J. T., TSANG, C. F. & RUTQVIST, J. 2008 A method for quick assessment of CO<sub>2</sub> storage capacity in closed and semi-closed saline formations. *Int. J. Greenh. Gas Control* **2**, 626–639.
- 625  
626
- 627 ZHU, Q., ZUO, D., ZHANG, S., ZHANG, Y., WANG, Y. & WANG, L. 2015 Simulation of geomechanical responses of reservoirs induced by CO<sub>2</sub> multilayer injection in the Shenhua CCS project, China. *Int. J. Greenh. Gas Control* **42**, 405–414.
- 628  
629

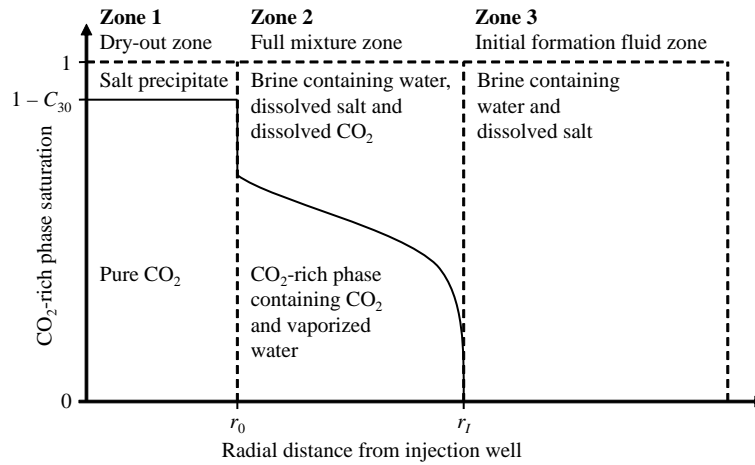


FIGURE 1. A schematic diagram illustrating the distribution of CO<sub>2</sub>, water and salt around a CO<sub>2</sub> injection well in a saline formation.

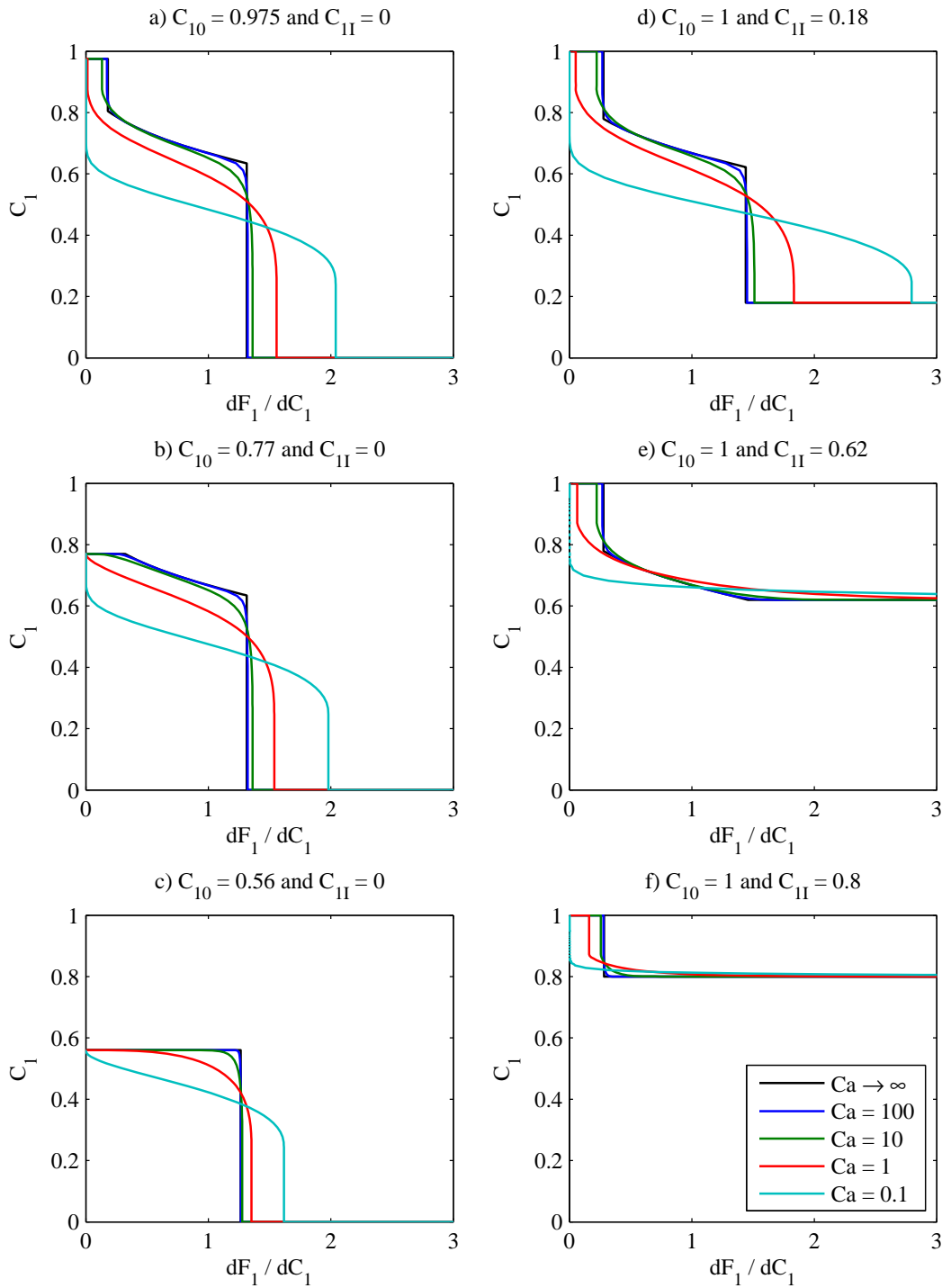


FIGURE 2. Sensitivity analysis based on gas-displacing-oil examples. The infinite  $Ca$  value curves were obtained from the method of characteristics solutions presented in Figs. 4.13 and 4.15 of Orr (2007). The finite  $Ca$  value curves were obtained using the pseudospectral solution documented in the current article.

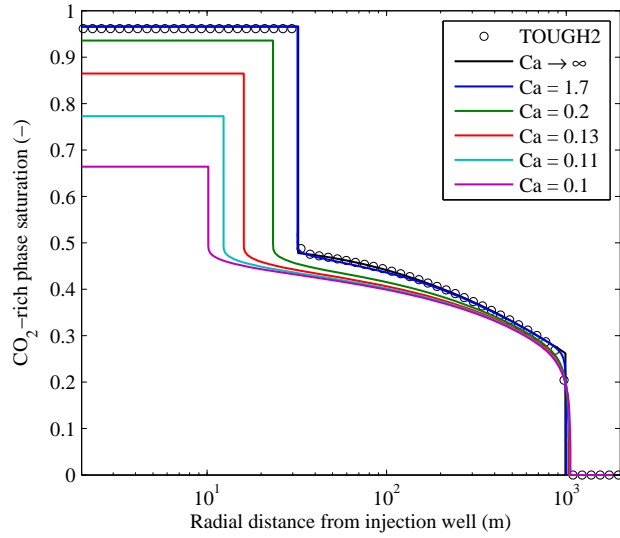


FIGURE 3. Plots of  $\text{CO}_2$  saturation against radial distance after injecting 4.73 Mt of  $\text{CO}_2$  whilst assuming a range of different capillary numbers,  $\text{Ca}$ . The TOUGH2 results are from the simulations previously presented by Mathias *et al.* (2013). Other associated model parameters are presented in Table 2. The results for  $\text{Ca} \rightarrow \infty$  were obtained using a method of characteristics solution, also presented by Mathias *et al.* (2013). The results for finite  $\text{Ca}$  values were obtained using the pseudospectral solution.

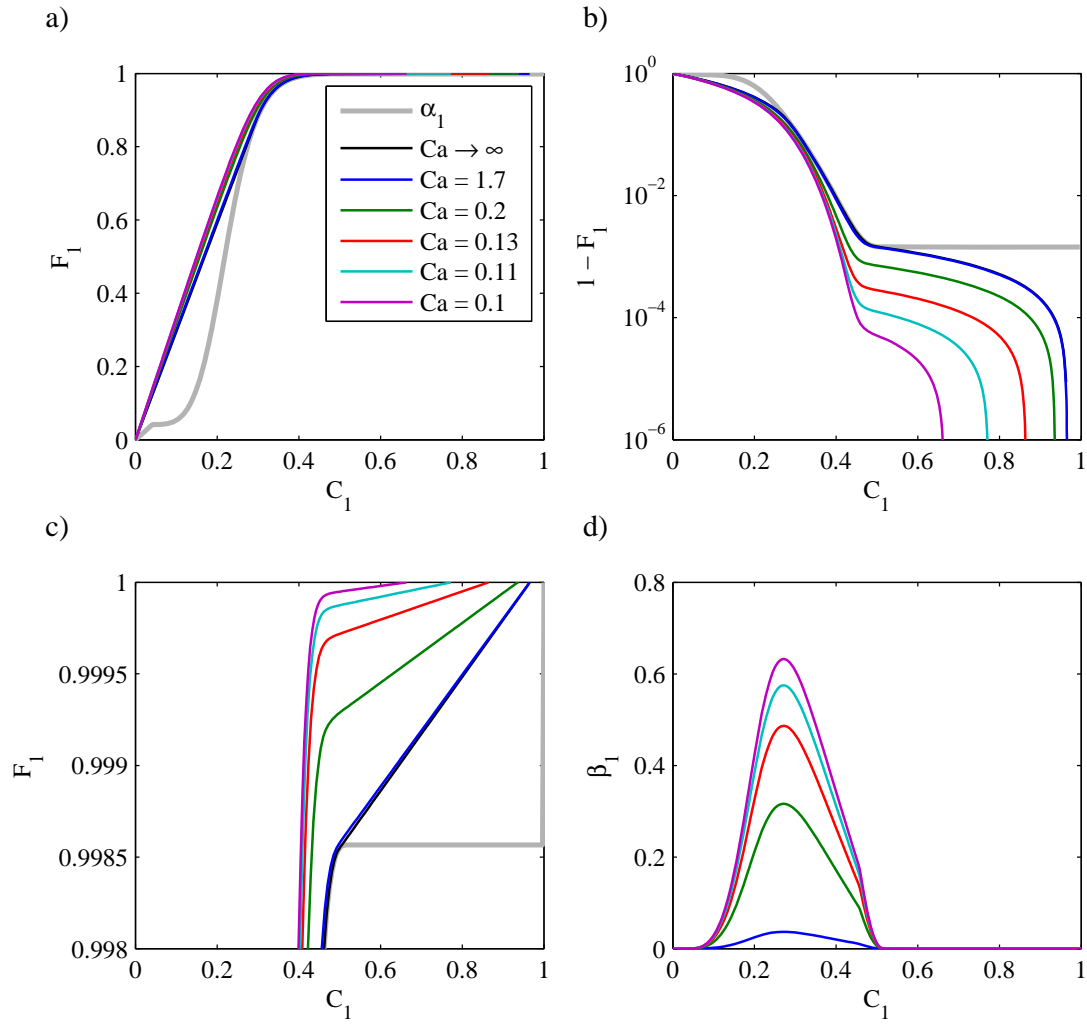


FIGURE 4. Plots of  $F_1$ ,  $\alpha_1$  and  $\beta_1$  against  $C_1$  for the simulation results presented in Fig. 3.

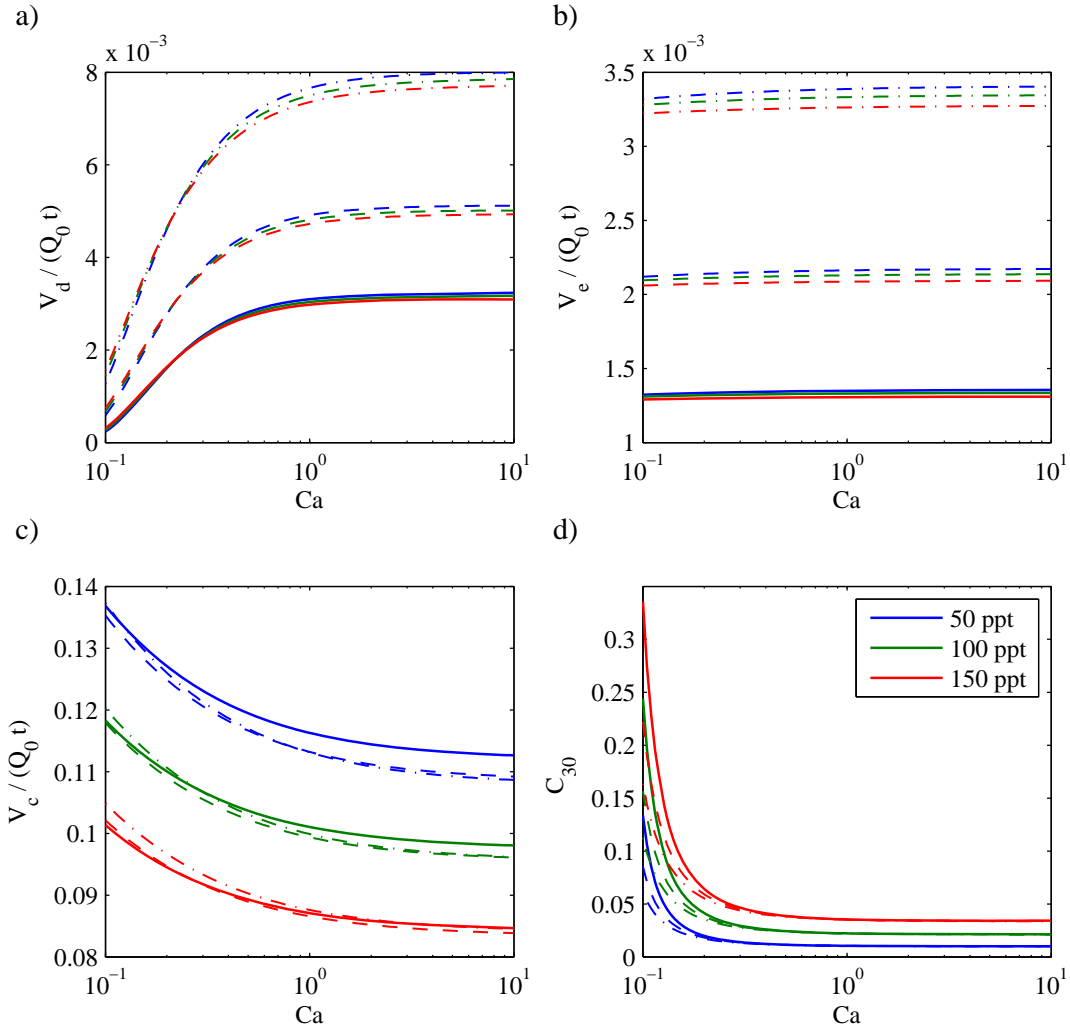


FIGURE 5. Sensitivity analysis based around the scenario presented in Fig. 3. The different colors relate to different brine salinities, as indicated in the legend. The solid lines, dashed lines and dash-dotted lines represent results obtained using fluid properties calculated assuming the saline formation exists at a depth of 1000 m, 1500 m and 2000 m, respectively (based on hydrostatic pressure conditions and a geothermal gradient of  $40^\circ\text{C}$  per km as in Table 3). a) shows plots of the ratio of dry-out zone volume ( $V_d$ ) to injected  $\text{CO}_2$  volume ( $Q_0 t$ ) against capillary number (Ca). b) shows plots of the ratio of volume of evaporated water ( $V_e$ ) to  $Q_0 t$  against Ca. c) shows plots of the ratio of volume of dissolved  $\text{CO}_2$  ( $V_c$ ) to  $Q_0 t$  against Ca. d) shows plots of precipitated salt volume fraction in the dry-out zone ( $C_{30}$ ) against Ca.

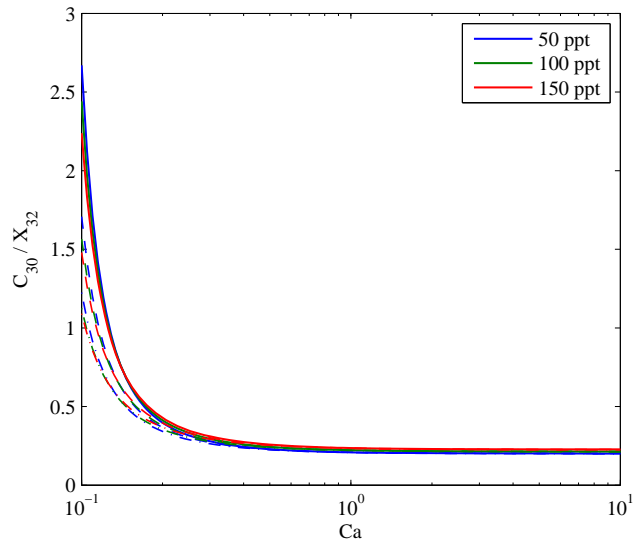


FIGURE 6. The same as Fig. 5d except that salt volume fraction,  $C_{30}$ , is divided by the salinity of the brine,  $X_{32}$ .

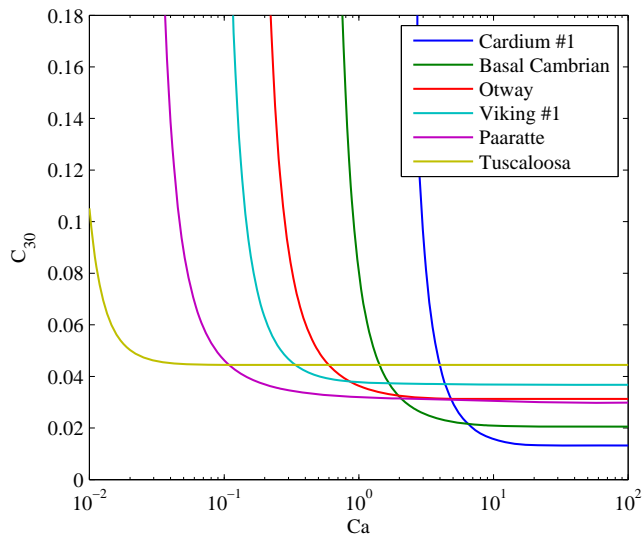


FIGURE 7. Plot of normalized precipitated salt volume fraction,  $C_{30}$ , against capillary number,  $Ca$ , using the 1000 m depth model scenario described in Tables 2 and 3 in conjunction with the different relative permeability parameters given in Table 4.